Geochimica et Cosmochimica Acta 346 (2023) 231–244

Contents lists available at ScienceDirect

Geochimica et Cosmochimica Acta

journal homepage: www.elsevier.com/locate/gca

# Competitive incorporation of Mn and Mg in vivianite at varying salinity and effects on crystal structure and morphology

L. Joëlle Kubeneck [a,*], Laurel K. ThomasArrigo [a], Katherine A. Rothwell [a], Ralf Kaegi [b], Ruben Kretzschmar [a]

[a] Soil Chemistry Group, Institute of Biogeochemistry and Pollutant Dynamics, Department of Environmental Systems Science, ETH Zürich, Universitätstrasse 16, CHN, CH-8092 Zürich, Switzerland
[b] Eawag, Swiss Federal Institute of Aquatic Science and Technology, Überlandstrasse 133, CH-8600 Dübendorf, Switzerland

ARTICLE INFO

*Article history:*
Received 17 September 2022
Accepted 27 January 2023
Available online 6 February 2023
*Associate editor:* Elizabeth Herndon

*Keywords:*
Ferrous phosphate minerals
Phosphorus burial
Isomorphic substitution
Mössbauer Spectroscopy
Electron microscopy

ABSTRACT

Vivianite, a ferrous phosphate mineral, can be an important phosphorus (P) sink in non-sulfidic, reducing coastal sediments. The Fe in the crystal structure of vivianite can be substituted by other divalent metal cations such as $Mn^{2+}$ or $Mg^{2+}$. Since Mg is much more abundant in coastal porewaters than Mn, the more frequent reports of Mn substitution in vivianites of coastal sediments has been suggested to indicate a preferential incorporation of Mn over Mg into the crystal structure of vivianite. However, although both Mn and Mg substitution in vivianite are environmentally relevant, it is yet unknown whether Mn or Mg is preferentially incorporated and how these isomorphic substitutions alter the crystal structure and morphology of vivianite, parameters which may influence vivianite reactivity. Here, we studied the incorporation of Mn and/or Mg in vivianites formed by co-precipitation at pH 7 in the presence of varying dissolved Mn and/or Mg concentrations and solution salinities resembling an estuarine gradient from 0 to 9 psu. In total, 19 different vivianites were synthesized, with up to 50% of Fe substituted by Mn and Mg. Thermodynamic equilibrium calculations showed that aqueous Mg speciation was altered with increasing salinity, while Mn speciation was less affected, likely explaining the preferential incorporation of Mn in the vivianite structure at higher salinities. $^{57}$Fe-Mössbauer spectroscopy revealed that both Mn and Mg were preferentially incorporated in the double-octahedral Fe position, at which intervalence charge transfer is possible during the oxidation of vivianite. In contrast to Mg, which is redox inactive, incorporated Mn can participate in heteronuclear intervalence charge transfer with Fe. Thus, incorporation of either cation may impact the reactivity of vivianite under oxidizing conditions in element specific ways. Results of complementary analyses including X-ray diffraction, electron microscopy and Fe K-edge X-ray absorption spectroscopy further showed that incorporation of Mn and/or Mg led to smaller particle size, increased crystal roughness and thinner crystals, as well as systematic changes in unit cell parameters. These observed changes in crystal morphology might impact the reactivity of vivianite in natural environments and thus the effect of cation incorporation in vivianite should be considered when studying Fe and P cycling in coastal sediments.



## 1. Introduction

Phosphorus (P) is an important nutrient for primary producers in aquatic ecosystems, but excessive concentrations can lead to eutrophication. The only way to remove bioavailable P from the water column is through sedimentation with subsequent burial (Froelich, 1988; Ruttenberg, 2003). Under reducing, non-sulfidic conditions, the ferrous iron phosphate mineral vivianite ($Fe_3(PO_4)_2{\cdot}8H_2O$) serves as a P sink in different environments, such as wetland soils as well as limnic and coastal sediments (see Rothe et al. (2016) for a comprehensive review on the topic). Although analytical detection and quantification of vivianite in environmental samples remains challenging, estimations derived from geochemical calculations for oligotrophic and eutrophic sulfide-poor coastal sediments containing vivianite suggest that 35–50% of total P may be bound in the form of vivianite in these sediments. Phosphorus may additionally be associated to organics, calcium minerals and ferric minerals (Egger et al., 2015; Kubeneck et al., 2021). Due to the low solubility of vivianite at circumneutral pH, it is considered to be a permanent P sink under non-sulfidic conditions in these environments (Thinnappan et al., 2008). Thus, the formation

* Corresponding author.
*E-mail address:* luisa.kubeneck@usys.ethz.ch (L. Joëlle Kubeneck).

https://doi.org/10.1016/j.gca.2023.01.029
0016-7037/

and subsequent burial of vivianite can have long-term positive effects on eutrophic aquatic ecosystems (Rothe et al., 2015; Lenstra et al., 2018).

Vivianite crystallizes in a monoclinic system with a layered structure in which stacking occurs along the b-axis of the unit cell (Fig. S1, Jeon et al. (2015)). Relatively weak hydrogen bonds between the $H_2O$ ligands connect each layer, leading to a perfect cleavage along the (010) surface and making the (010) surface thermodynamically the most stable (McCammon and Burns, 1980; Jeon et al., 2015). The ferrous iron atoms ($Fe^{2+}$ is denoted for simplicity as Fe in this study) are located in two distinct octahedral sites (Mori and Ito, 1950). One Fe atom is present in an isolated octahedron ($Fe_A$ position), while the other two Fe atoms are located in a double octahedron ($Fe_B$ position), which shares a common O–O edge (Fig. S1, Mori and Ito (1950)). The very short interatomic distance (~2.95 Å) between the two Fe atoms in the $Fe_B$ position enables intervalence charge transfer between the two Fe atoms in case of differing oxidation state (Allen and Hush, 1967). Investigation on the oxidation of vivianite has revealed that oxidation rates between the crystallographic sites are similar until about 10% of the Fe has been oxidized. However, with increasing ferric concentration, the Fe at the $Fe_A$ site is preferentially oxidized relative to the Fe located in the $Fe_B$ site. This is related to the observation that when one Fe atom in the $Fe_B$ position has been oxidized the other Fe atom is relatively unreactive with respect to oxidation due to intervalence charge transfer (McCammon and Burns, 1980). This stabilization might explain the observation that even after 375 days under oxic conditions only 50% of the Fe in the vivianite structure was oxidized. Up to this oxidation level the vivianite structure is also still intact and would be identified as vivianite by XRD (Rouzies and Millet, 1993).

In the environment, Fe in the vivianite structure can be substituted by various divalent metal cations such as manganese (Mn), magnesium (Mg), and zinc (Zn; Rothe et al. (2016) and references therein). Laboratory studies have shown that upon microbial reductive dissolution, nickel (Ni) and cobalt (Co) previously adsorbed and incorporated to ferric minerals were adsorbed and incorporated in the secondary vivianite, suggesting the ability of vivianite to immobilize trace metals (Zachara et al., 2001). Nevertheless, the most common isomorphic substitution in vivianite occurs with Mn and Mg in the environment (Rothe et al. (2016) and references therein). In oligohaline and mesohaline coastal regions, Mn substitution has been more frequently reported than Mg substitution (Egger et al., 2015; Lenstra et al., 2018; Kubeneck et al., 2021). This is counter-intuitive considering that Mg is, after sodium, the second most abundant cation in seawater (Kester et al., 1967) and Mg concentrations are, therefore, generally higher than Mn concentrations in coastal waters. This discrepancy between the composition of the aqueous solution and the solid phase has been suggested to indicate that Mn may be preferentially incorporated into the vivianite crystal structure (Kubeneck et al., 2021). Another variable that changes along the freshwater-seawater continuum is salinity. Substitution of Mg in calcite has been shown to be influenced by salinity (Berner, 1975; Tang et al., 2012). Hence, salinity might also affect the relative amounts of Mn and/or Mg incorporated in the vivianite crystal structure. Although both Mn and Mg incorporation in vivianite are environmentally relevant, it is yet unknown whether Mn or Mg are preferentially incorporated into the vivianite structure at varying salinity.

Isomorphic substitution changes the unit-cell dimensions of various ferric and ferrous minerals (e.g. Gerth 1990; Alvarez et al. 2006; Liu et al. 2019) and may also alter crystallite size, crystal morphology, surface area and solubility (Trolard and Tardy, 1987; Alvarez et al., 2006; Liu et al., 2018a, 2019), surface chemistry (Ainsworth et al., 1989), and the rates of proton-promoted and reductive dissolution rates (Torrent et al., 1987; Ekstrom et al., 2010) of various Fe minerals such as goethite, hematite and siderite. While the effects of isomorphic substitution on crystal structure, crystallite size and morphology have been studied for various other Fe minerals, it remains unknown how incorporation of Mn and/or Mg in vivianite affects the crystal structure and morphology of vivianite. Additionally, it remains elusive in which Fe position Mn and/or Mg incorporation occurs. For example, if isomorphic substitution occurs in the $Fe_B$ position, it could impact the ability to carry out intervalence charge transfer, with possible implications for the stabilization of vivianite against oxidation.

Considering the importance of vivianite as a P burial sink in certain environments, it is essential to improve our understanding on how environmental parameters, such as salinity, affect the isomorphic substitution of Mn and/or Mg in vivianite. In addition, it is of interest to assess in which Fe position Mn and/or Mg are preferentially incorporated and the subsequent effects that both salinity and isomorphic substitution have on crystal structure and morphology. Detailed knowledge about how the crystal structure of vivianite changes with isomorphic substitution and with varying salinity will further improve our understanding of how isomorphic substitution changes mineral reactivity and stability. Consequently, in this study we investigated the competitive substitution of Mn and/or Mg in vivianite at varying salinity chosen to resemble an oligohaline and mesohaline estuarine gradient (0–9 psu). To this end, we synthesized 19 different vivianites at varying salinity and aqueous Mn and/or Mg concentrations. The different vivianites were analyzed by $^{57}$Fe-Mössbauer spectroscopy to identify the Fe atom position in which preferential incorporation occurs. By combining X-ray diffraction (XRD), electron microscopy (EM) and Fe K-edge X-ray absorption spectroscopy (XAS) we identified changes in crystal morphology, unit cell dimensions and atom positions in vivianites with different amounts of Mn and/or Mg incorporation.

## 2. Materials and methods

### 2.1. Vivianite synthesis

All solutions were prepared using analytical grade chemicals with de-oxygenated and $CO_2$-free ultra-pure water (UPW; Milli-Q, Millipore, >18.2 MΩ·cm). All glassware used for vivianite synthesis was acid-washed (10% hydrochloric acid (HCl), v/v) for 24 h and then rinsed thoroughly with UPW prior to use.

Nineteen different vivianites were synthesized in an anoxic chamber (MBraun, UNIlab Plus, $N_2$ atmosphere, <1 ppm (v/v) $O_2$) at room temperature by co-precipitation, under conditions covering a salinity range of 0 to 9 psu and (Mn + Mg)/(Mn + Mg + Fe) molar ratios of 0–0.52 (Table 1). The vivianites were synthesized at four different salinities (0, 3, 6 and 9 psu) and with low, medium or high Mn and/or Mg concentrations (4.56, 9.14 and 13.70 mM, respectively). Abbreviations for the synthesized vivianites can be found in Table 1 and contain information about the Mn and/or Mg content (low = 1, medium = 2, high = 3) and salinity of the synthesis solutions. For the synthesis of Fe-pure vivianite (V_pure_0-psu, Table 1), 900 mL of a 25 mM $FeSO_4$ stock solution was prepared and continuously stirred (300 rpm), while 100 mL of a 391 mM $Na_2HPO_4$ stock solution was added. To synthesize minerals with varying Mn and/or Mg concentrations at different salinity, 900 mL of stock solutions containing 25 mM $FeSO_4$ and varying concentrations of $MnCl_2$ or $MgCl_2$ (4.56, 9.14 and 13.70 mM), and/or different amounts of artificial seawater (35 psu, prepared after Kester et al. (1967)) were prepared under continuous stirring (300 rpm) to which 100 mL of a 391 mM $Na_2HPO_4$ stock solution was added. Sulfate and chloride concentrations in the final co-precipitation suspensions were elevated in comparison to natural

**Table 1**
Synthesis conditions of 19 different vivianites, initial aqueous chemical speciation conditions for two key species ($MgHPO_4$ and $MgCl^+$) and saturation indices with respect to vivianite. For all syntheses, 25 mM $Fe^{2+}$ and 58.75 mM $PO_4^{3-}$ were present. $Mn^{2+}$ was added in form of a $MnCl_2$ solution and $Mg^{2+}$ was added either with artificial seawater or added in form of a $MgCl_2$ solution (*). The mineral formula was calculated based on the determined elemental composition of the synthesized vivianites (after acid dissolution) by ICP-OES. Ratios presented in this table refer to molar ratios.

| Vivianite no. | Abbreviation | Mineral formula solid phase | Salinity [psu] | $Mn^{2+}$ [mM] | $Mg^{2+}$ [mM] | $\frac{Mn}{Mn+Fe}$ (aq) | $\frac{Mg}{Mg+Fe}$ (aq) | $\frac{Mg+Mn}{Mg+Mn+Fe}$ (aq) | $MgHPO_4$ (aq) [% of total $PO_4^{3-}$ (aq)] | $MgCl^+$ [% of total $Mg_{(aq)}$] | Saturation index |
|---|---|---|---|---|---|---|---|---|---|---|---|
| 1 | V_pure_0psu | $Fe_{3.3}(PO_4)_2{\cdot}8H_2O$ | 0 | 0.00 | 0.00 | 0.00 | 0.00 | 0.00 | | | 13.2 |
| 2 | V_Mg1_0psu | $Fe_{2.82}Mg_{0.46}(PO_4)_2{\cdot}8H_2O$ | 0 | 0.00 | 4.56(*) | 0.00 | 0.15 | 0.15 | 3.6 | 0.5 | 13.2 |
| 3 | V_Mg2_0psu | $Fe_{2.44}Mg_{0.81}(PO_4)_2{\cdot}8H_2O$ | 0 | 0.00 | 9.14 (*) | 0.00 | 0.27 | 0.27 | 5.3 | 0.7 | 13.2 |
| 4 | V_Mg3_0psu | $Fe_{2.18}Mg_{1.05}(PO_4)_2{\cdot}8H_2O$ | 0 | 0.00 | 13.70 (*) | 0.00 | 0.35 | 0.35 | 9.6 | 1.7 | 13.2 |
| 5 | V_Mg1_3psu | $Fe_{2.84}Mg_{0.44}(PO_4)_2{\cdot}8H_2O$ | 3 | 0.00 | 4.56 | 0.00 | 0.15 | 0.15 | 3.0 | 2.5 | 13.2 |
| 6 | V_Mg2_6psu | $Fe_{2.56}Mg_{0.64}(PO_4)_2{\cdot}8H_2O$ | 6 | 0.00 | 9.14 | 0.00 | 0.27 | 0.27 | 4.9 | 4.8 | 13.2 |
| 7 | V_Mg3_9psu | $Fe_{2.38}Mg_{0.72}(PO_4)_2{\cdot}8H_2O$ | 9 | 0.00 | 13.70 | 0.00 | 0.35 | 0.35 | 6.8 | 7.2 | 13.2 |
| 8 | V_Mn1_0psu | $Fe_{2.82}Mn_{0.50}(PO_4)_2{\cdot}8H_2O$ | 0 | 4.56 | 0.00 | 0.15 | 0.00 | 0.15 | | | 13.2 |
| 9 | V_Mn2_0psu | $Fe_{2.44}Mn_{0.84}(PO_4)_2{\cdot}8H_2O$ | 0 | 9.14 | 0.00 | 0.27 | 0.00 | 0.27 | | | 13.2 |
| 10 | V_Mn3_0psu | $Fe_{2.16}Mn_{1.12}(PO_4)_2{\cdot}8H_2O$ | 0 | 13.70 | 0.00 | 0.35 | 0.00 | 0.35 | | | 13.2 |
| 11 | V_Mn1_Mg1_3psu | $Fe_{2.38}Mn_{0.44}\ Mg_{0.34}(PO_4)_2{\cdot}8H_2O$ | 3 | 4.56 | 4.56 | 0.15 | 0.15 | 0.27 | 2.7 | 3.1 | 13.2 |
| 12 | V_Mn2_Mg1_3psu | $Fe_{2.19}Mn_{0.76}\ Mg_{0.30}(PO_4)_2{\cdot}8H_2O$ | 3 | 9.14 | 4.56 | 0.27 | 0.15 | 0.35 | 2.5 | 3.8 | 13.2 |
| 13 | V_Mn3_Mg1_3psu | $Fe_{1.94}Mn_{1.02}\ Mg_{0.28}(PO_4)_2{\cdot}8H_2O$ | 3 | 13.70 | 4.56 | 0.35 | 0.15 | 0.42 | 2.4 | 4.4 | 13.3 |
| 14 | V_Mn1_Mg2_6psu | $Fe_{2.26}Mn_{0.40}\ Mg_{0.54}(PO_4)_2{\cdot}8H_2O$ | 6 | 4.56 | 9.14 | 0.15 | 0.27 | 0.35 | 4.1 | 5.4 | 13.2 |
| 15 | V_Mn2_Mg2_6psu | $Fe_{1.94}Mn_{0.76}\ Mg_{0.54}(PO_4)_2{\cdot}8H_2O$ | 6 | 9.14 | 9.14 | 0.27 | 0.27 | 0.42 | 4.4 | 6.1 | 13.2 |
| 16 | V_Mn3_Mg2_6psu | $Fe_{1.76}Mn_{0.94}\ Mg_{0.50}(PO_4)_2{\cdot}8H_2O$ | 6 | 13.70 | 9.14 | 0.35 | 0.27 | 0.48 | 4.3 | 6.9 | 13.3 |
| 17 | V_Mn1_Mg3_9psu | $Fe_{2.14}Mn_{0.38}\ Mg_{0.64}(PO_4)_2{\cdot}8H_2O$ | 9 | 4.56 | 13.70 | 0.15 | 0.35 | 0.42 | 6.6 | 7.8 | 13.2 |
| 18 | V_Mn2_Mg3_9psu | $Fe_{1.78}Mn_{0.68}\ Mg_{0.64}(PO_4)_2{\cdot}8H_2O$ | 9 | 9.14 | 13.70 | 0.27 | 0.35 | 0.48 | 6.4 | 8.9 | 13.3 |
| 19 | V_Mn3_Mg3_9psu | $Fe_{1.78}Mn_{0.94}\ Mg_{0.47}(PO_4)_2{\cdot}8H_2O$ | 9 | 13.70 | 13.70 | 0.35 | 0.35 | 0.52 | 5.9 | 9.2 | 13.3 |

seawater conditions at specific salinities as both anions were additionally added through the cation stock solutions. All solutions were supersaturated with respect to vivianite (saturation index (SI) ~13, Table 1) to induce nucleation and crystal growth at pH 7 (Liu et al., 2018b). $PO_4^{3-}$ was added in excess in order to scavenge all $Fe^{2+}$ from solution. After mixing the solutions, the pH was close to 7 and was, within the first 5 min, readjusted to 7.0 ± 0.1 with drop-wise additions of 2 M NaOH (0–10 mL depending on the vivianite synthesized) and remained stable thereafter. Upon mixing of the solutions, a white precipitate appeared immediately and the suspensions were continuously stirred at 300 rpm for 24 h. Since vivianite is sensitive to light (Frost et al., 2004), the syntheses were carried out in aluminum (Al)-covered amber glass flasks in a dark room.

After 24 h, 9 mL of the well-mixed suspensions were taken (in duplicate) and acidified with 1 mL of 1 M HCl for determination of total elemental composition by inductively coupled plasma optical emission spectroscopy (ICP-OES, Agilent 5100). An additional 9 mL aliquot was taken and filtered with a 0.22 µm nylon filter and the filtrate stabilized with 1 mL of 1 M HCl. The remaining suspensions were then filtered (0.45 µm, nylon) to recover the solid-phase material. A 9 mL sample of the 0.45 µm filtrate was also kept and stabilized with 1 mL of 1 M HCl. The elemental composition determined by ICP-OES of the 0.45 and 0.22 µm filtrates was the same within instrumental error, indicating the absence of vivianite crystals with a size of 0.22–0.45 µm. The recovered vivianite (4–8 g) was washed with 1 L UPW and dried under dark and anoxic conditions. The dried vivianite was gently homogenized with an agate mortar and pestle and stored under dark and anoxic conditions.

In addition, a pure manganese phosphate (Mn-phosphate) mineral was synthesized as a reference material for further characterization. The same protocol as for the Fe-pure vivianite (V_pure_0psu, Table 1) was applied but Fe was replaced by Mn. Thus, the mineral was synthesized by co-precipitation from a solution containing 25 mM $Mn^{2+}$ and 58.75 mM $PO_4^{3-}$.

### 2.2. Vivianite characterization

#### 2.2.1. Elemental composition

Elemental composition of the acidified co-precipitation suspensions was determined by ICP-OES for Fe, Mn, Mg, Na, Ca, K, Sr, P and S. All P and S were assumed to be present as $PO_4^{3-}$ and $SO_4^{2-}$, respectively. The elemental composition of the co-precipitation suspension was used for thermodynamic equilibrium calculations (see Section 2.2.2). To determine the bulk elemental composition of the synthesized vivianites, ~10 mg of each dried vivianite was dissolved (in duplicate) in 10 mL of 1 M HCl. The solution was subsequently analyzed by ICP-OES for Fe, Mn, Mg, Na, Ca, K, Sr, P and S.

#### 2.2.2. Thermodynamic equilibrium calculations

Elemental chemical speciation and SI of possible solids (at 25°C) were calculated with VisualMINTEQ (Version 3.1) using the default database (thermo.vdb, comp_2008.vdb) and elemental concentrations of the co-precipitation suspensions as input (Section 2.2.1). The solution pH was fixed to 7.0 and ionic strength was calculated, using the Davies equation for ion activity corrections. Ionic strength of the initial solutions varied between 0.15 and 0.33 M, which is within the valid range of the Davies equation (Stumm and Morgan, 2012). The SI and chemical speciation results reported in this paper are based on calculations in which oversaturated solids were not allowed to precipitate. Additional calculations allowing precipitation of oversaturated solids in each iteration step were performed to identify which other solid phases besides vivianite may have formed (Section S2).

#### 2.2.3. X-ray diffraction with Rietveld fitting

Powder XRD patterns for the 19 different vivianites and the Mn-phosphate were collected with a Bruker D8 ADVANCE diffractometer equipped with a high-resolution energy-dispersive one-dimensional (1-D) detector (LYNXEYE) and Cu anode source ($k_{\alpha1}$ = 1.5406 Å; $k_{\alpha2}$ = 1.54439 Å). A small aliquot of dried mineral powder was re-suspended in ethanol, deposited onto a polished

silicon wafer (Sil'tronix Silicon Technologies, France), and dried in the dark anoxic chamber, leading to evenly dispersed crystal deposit. To maintain anoxic conditions during XRD analysis, a Plexiglas dome equipped with an anti-scatter knife edge (Bruker, A100B138-B141) was used. The diffractograms were collected in the dark in Bragg-Brentano geometry in the 5–90° 2θ range with a 0.02° step size and an acquisition time of 2 s per step. The diffractograms were analyzed by Rietveld fitting in TOPAS (V.5.0; Bruker, Germany) based on CIF files for vivianite (Inorganic Crystal Structure Database (ICSD), #423390, (Capitelli et al., 2012)), Mg-substituted vivianite (ICSD, #423389, (Capitelli et al., 2012)) and $Mn_3(PO_4)_2{\cdot}3H_2O$ (JCPDS card no. 00-003-0426). For all vivianites, the unit cell parameters were fitted and crystallite sizes were obtained using a Lorentzian peak function and reported as the volume weighted size parameter LVol-IB in TOPAS. In addition, as a comparison, crystallite thickness was obtained by a single peak fit in the (0 1 0) plane direction (peak at ~13.4° 2θ), reflecting the thickness of the crystallites perpendicular to the plane. Instrumental peak broadening was accounted for using NIST SRM 660c (LaB6) as a reference with a crystallite size of 800 nm. Preferred orientation along the (0 1 0) plane was included in the fit based on the March-Dollase equation implemented in TOPAS (Dollase, 1986) and the background was modelled by the Chebyshev polynomial function (order set to 20).

The presence of Mg in the vivianite crystal structure changes the intensity of various diffraction peaks (Fig. S6), allowing an estimate of the Mg/(Mg + Fe) ratio in Mg-containing vivianites to be made. Examples of changes in the diffraction region of 15–40° 2θ are presented in Fig. S6. For Mg-containing vivianites, site occupancy factors for both cationic sites ($Fe_A$ and $Fe_B$) in the vivianite structure were refined with respect to Fe and Mg fractions in TOPAS, assuming full occupancy for both cationic sites. Since Mn and Fe have similar X-ray scattering factors (Colliex et al., 2006), the incorporation of Mn into vivianite does not significantly change the relative peak intensities. Consequently, Mn substitution cannot be quantified based on changes in peak intensities by Rietveld fitting.

*2.2.4. Fe XAS analysis*

Five vivianites of this study (V_pure_0psu, V_Mg3_0psu, V_Mg3_9psu, V_Mn3_0psu and V_Mn3_ Mg3_9psu, Table 1) were analyzed by bulk Fe K-edge near-edge structure and extended X-ray absorption fine structure (XANES and EXAFS, respectively) spectroscopy at the LUCIA beamline of SOLEIL (Saint-Aubin, France). The dried vivianites were pressed into 1.3 cm pellets and sealed with Kapton tape. To prevent Fe oxidation, the pellets were prepared in an anoxic glovebox in a dark room and doubly sealed in Al-bags for transport to the synchrotron. Directly prior to sample mounting, the Al-sealed bags were opened in ambient air and the Kapton-sealed pellet was mounted on a sample holder. The mounted sample was then inserted into a cryostat (He(l), ~70 K) and measured in transmission mode using a Si(1 1 1) monochromator calibrated to the first-derivative maximum of the K-edge absorption spectrum of a metallic Fe foil (7112 eV). Mirrors eliminated higher harmonics in the incoming beam. Three to five scans of each vivianite were collected and merged. For data analysis, all spectra were energy calibrated, pre-edge subtracted, and post-edge normalized in Athena (Ravel and Newville, 2005). The edge energy, $E_0$, was defined as the first maximum of the main absorption edge in the first XANES derivative. Fourier transforms of $k^3$-weighted Fe EXAFS spectra were calculated over a k-range of 2–11.5 $Å^{-1}$ applying a Kaiser-Bessel window function width of 3 $Å^{-1}$. The frequency cut-off parameter, Rbkg, was set to 1.

Shell-fit analyses of $k^3$-weighted Fe EXAFS spectra were performed in R-space using Artemis (Ravel and Newville, 2005). Theoretical phase-shift and amplitude functions were derived with FEFF6 (Zabinsky et al., 1995) and atomic positions from the crystal structure of vivianite (ICSD, #423390, (Capitelli et al., 2012) and $Mn_3(PO_4)_2{\cdot}3H_2O$ (JCPDS card no. 00-003-0426, for V_Mn3_0psu). To determine the passive amplitude reduction factor ($S_0^2$), the first-neighbor shell (R + ΔR = 1.0–2.2 Å) was fitted with a Fe–O bond with a coordination number (CN) of 6 for V_pure_0psu. The determined $S_0^2$ was used for all subsequent fits (reported Table 2). The substituted vivianites were then fit with an initial R-space fit of the first Fourier-transform peak conducted over R + ΔR = 1.0 to 2.2 Å to determine the CN of the first Fe–O bond. After fixing the determined CN for the Fe–O bonds, shell-fits were extended to 6.0 Å. To verify that the addition of certain paths improved the EXAFS fit significantly, F-Tests based on determined R-factors were used to compare different fitting models (Table S7, Downward et al. (2007); Ravel and Newville (2005)). As the crystal structure of vivianite did not change fundamentally with substitution, as visible by the XRD patterns (Fig. S4), the substituted vivianites were all fitted with the same fitting model (Section S6).

*2.2.5. Electron microscopy with energy dispersive X-ray (EDX) analysis*

Samples V_pure_0psu, V_Mg3_0psu, V_Mg3_9psu, V_Mn1_0psu, V_Mn3_0psu and V_Mn3_ Mg3_9psu (Table S4) were investigated by EM coupled to EDX to gain insights into crystal morphology and elemental distribution. Samples were prepared by suspending dried vivianite powder in de-oxygenated UPW (~3 μg/mL) in an anoxic chamber. The suspension (15 mL) was filtered on a 13 mm (0.2 μm) isopore membrane filter (polycarbonate) to collect ~45 μg vivianite on the filter. The filters were air-dried in the dark anoxic chamber. Afterwards, the dried filters were doubly sealed in Al-bags for transport to the microscopy location. The filters containing the deposited particles were coated with 5 nm of a platinum/palladium (80 Pt/20 Pd) and the secondary electron signal was used for imaging. Samples were investigated using a scanning electron microscope (SEM, Gemini 460, Zeiss and Nova Nanosem 230, FEI with an Oxford EDX system). The SEM was operated at an accelerating voltage of 1–3 kV.

*2.2.6. $^{57}$Fe-Mössbauer spectroscopy*

$^{57}$Fe-Mössbauer spectra were collected using a $^{57}$Co/Rh γ-radiation source in constant acceleration mode in transmission setup (WissEl,Wissenschaftliche Elektronik GmbH). Samples were mounted on mixed cellulose millipore filter membranes (0.22 μm) and wrapped in Kapton tape in the anoxic chamber, where they were kept until immediately before analysis. The samples were measured at 77 K inside a closed-cycle exchange gas (He) cryostat (Janis cryogenics). The temperature of 77 K was chosen in order to be able to quantify the contribution of Fe atoms bound in the $Fe_A$ and $Fe_B$ positions, as well as compare the fitting parameters to previously published data (Dyar et al., 2014; Etique et al., 2021). Spectra were calibrated with α-Fe(0) foil at 295 K and the line width was set according to the inner line broadening of the calibration foil at 295 K. In addition, the collected spectra were normalized to 1 with respect to absorption. Fitting was undertaken using Recoil software (University of Ottawa, Canada; Rancourt and Ping (1991)) using Voigt spectral lines.

## 3. Results

### 3.1. Crystal morphology and size

Secondary electron (SE) images (Fig. 1, S9–S14) showed that the composition of the matrix modified the morphology of the crystallizing vivianite. The crystal size generally decreased with Mn and/or Mg substitution based on visual observations of the SE images. This trend is in agreement with fitted crystallite sizes based on

**Table 2**
Parameters determined for shell fits of $k^3$-weighted Fe K-edge EXAFS spectra.[a]

| | | V_pure_0psu | V_Mg3_0psu | V_Mg3_9psu | V_Mn3_0psu | V_Mn3_Mg3_9psu |
|---|---|---|---|---|---|---|
| Fe–O1 | CN[b] | **6.0** | **5.9** | **5.7** | **4.9** | **5.7** |
| | R(Å)[c] | 2.12 (0.01) | 2.13 (0.01) | 2.12 (0.01) | 2.11 (0.01) | 2.29 (0.01) |
| Fe–Fe1 | CN | 1.2 (0.2) | 1.0 (0.2) | 1.0 (0.2) | 0.5 (0.2) | 1.3 (0.2) |
| | R(Å) | 3.02 (0.01) | 3.04 (0.02) | 3.02 (0.01) | 3.05 (0.03) | 2.90 (0.01) |
| Fe–P | CN | 1.1 (0.4) | 1.8 (0.4) | 1.6 (0.4) | 1.9 (0.5) | 1.4 (0.4) |
| | R(Å) | 3.34 (0.04) | 3.33 (0.02) | 3.33 (0.02) | 3.36 (0.02) | 3.09 (0.03) |
| Fe-O2 | CN | 4.3 (1.7) | 4.7 (1.5) | 4.0 (1.2) | | 5.3 (1.3) |
| | R(Å) | 3.95 (0.03) | 3.95 (0.02) | 3.96 (0.02) | | 4.04 (0.02) |
| Fe–O–O | CN | 10.7 (8.4) | 15.1 (9.6) | 15.7 (9.3) | 5.8 (4.2) | 6.9 (4.2) |
| | R(Å) | 4.44 (0.03) | 4.44 (0.03) | 4.44 (0.03) | 4.47 (0.03) | 4.57 (0.02) |
| Fe–Fe2 | CN | 3.9 (0.8) | 2.3 (0.6) | 2.5 (0.6) | 1.7 (1.3) | 3.1 (0.9) |
| | R(Å) | 4.68 (0.02) | 4.66 (0.02) | 4.67 (0.02) | 4.74 (0.03) | 4.71 (0.02) |
| Fe–Fe3 | CN | 1.9 (1.0) | 1.0 (0.8) | 1.3 (0.7) | | 1.3 (0.9) |
| | R(Å) | 5.21 (0.03) | 5.22 (0.05) | 5.22 (0.03) | | 5.31 (0.05) |
| Fe–Fe4 | CN | 3.0 (1.1) | 1.6 (1.0) | 2.1 (0.9) | | 1.8 (1.1) |
| | R(Å) | **5.57** | **5.57** | **5.57** | | 5.53 (0.04) |
| Fe–Fe5 | CN | 6.5 (1.4) | 3.8 (1.3) | 4.3 (1.1) | 2.1 (1.2) | 4.8 (1.4) |
| | R(Å) | 6.23 (0.02) | 6.23 (0.02) | 6.22 (0.02) | 6.24 (0.04) | 6.11 (0.02) |
| Fe–Mn1[d] | CN | | | | 1.2 (0.3) | |
| | R(Å) | | | | 3.64 (0.02) | |
| Fe–Mn2[e] | CN | | | | 1.2 (1.0) | |
| | R(Å) | | | | 5.01 (0.05) | |
| $\sigma^2$[f] | Fe–Fe1-5 | **0.006** | **0.006** | **0.006** | **0.008** | **0.006** |
| | Fe–P | **0.006** | **0.006** | **0.006** | **0.006** | **0.006** |
| | Fe–O1 | **0.008** | **0.008** | **0.008** | **0.008** | **0.008** |
| | Fe–O2 | **0.007** | **0.007** | **0.007** | **0.007** | **0.007** |
| | Fe–O–O | 0.012 (0.010) | 0.015 (0.010) | 0.018 (0.010) | 0.007 (0.007) | 0.004 (0.005) |
| | Fe–Mn1-2 | | | | **0.006** | |
| $E_0$[g] (eV) | 2.49 (0.85) | 2.23 (0.77) | 2.20 (0.71) | 1.41 (0.89) | 2.91 (0.78) | |
| R-factor[h] | 0.015 | 0.012 | 0.011 | 0.017 | 0.014 | |
| Reduced $\chi^2$[i] | 113 | 40 | 152 | 140 | 99 | |

[a] The passive amplitude reduction factor, $S_0^2$, was set to 0.97 (see Section 2.2.4 for explanation how $S_0^2$ was determined). Parameter uncertainties are presented for the last significant figure.
[b] Path degeneracy (coordination number, CN).
[c] Mean-half path length. For path distances, CN and $\sigma^2$ marked in bold, the values were fixed.
[d,e] Fe–Mn path is taken from $Mn_3(PO_4)_2{\cdot}3H_2O$ (JCPDS card no. 00–003-0426) and thus is unique to V_Mn3_0psu.
[f] The Debye-Waller parameters.
[g] Energy-shift parameter.
[h] Normalized sum of squared residuals ($\Sigma_i$ ($data_i$ – $fit_i$)$^2$/$\Sigma_i$ $data^2$).
[i] Fit accuracy; reduced $\chi^2 = (N_{idp}/N_{pts})\,\Sigma_i(data_i - fit_i/\varepsilon_i)^2(N_{idp}/N_{var})^{-1}$. $N_{idp}$, $N_{pts}$, and $N_{var}$ are respectively, the number of independent data points in the model fit (29.5), the total number of data points (196) and the number of fitted variables (17 for V_Mn3_0psu, 19 for V_Mn3_Mg3_9psu and 18 for the others). $\varepsilon_i$ is the uncertainty of the $i^{th}$ data point.

Rietveld fitting of the XRD patterns of vivianite (reported as LVol-IB [nm], Table S2) for the whole collected diffraction range (values ranging from 51 nm to 168 nm) and a single peak fit in (0 1 0) plane direction (values ranging from 48 nm to 127 nm), representing the thickness of vivianite crystallites along the c-axis (Fig. S1).

Fe-pure vivianite (V_pure_0psu, Table 1) was characterized by crystals with an elongated rhomboid shape (Fig. 1AB, S9). The single crystal surface and prismatic edges were generally smooth. The appearance of steps was clearly visible, which resulted in a further twinning and intergrowth of single crystals (Fig. S9A). Besides single crystals, lamellar lenticular twinned crystals and stellate rosettes with a bladed structure were common (Fig. S9). Single crystals had a crystal size of ~5–10 μm along the b-axis and stellate rosettes had typically a size of 10 to 15 μm (Fig. 1AB, S9). The Rietveld fitted crystallite size (LVol-IB) was 132 nm and 127 nm for the whole range and single peak fit (along the c-axis of the vivianite crystal), respectively (Table S2).

Mn incorporation at 0 psu (V_Mn1_0psu and V_Mn3_0psu, Table 1, Fig. 1CD, S12, S13) did not greatly change the shape of the stellate rosettes in comparison to V_pure_0psu. Low Mn content (V_Mn1_0psu, Fig. S12) resulted in crystals appearing thicker along the c-axis than the Fe-pure vivianite crystals, which is also supported by the determined crystallite size of 181 nm along the c-axis (Table S2). Higher Mn substitution (V_Mn3_0psu, Fig. 1CD, S13), however, resulted in pits in the crystals, as visible in Fig. 1D. The stellate rosettes had a crystal size of ~8–15 μm and thus were slightly smaller than the crystals of V_pure_0psu. This observation is also supported by the determined crystallite size which was, with 88 nm, smaller than the V_pure_0psu crystallite size (LVol-IB). SE images of V_Mn3_0psu also indicated the presence of another mineral phase with a less distinct crystal morphology (Fig. 1CD, S8, S13). The composition of this second phase is discussed in further detail in Section 3.3.

The incorporation of Mg at 0 psu (V_Mg3_0psu, Table 1) led to changes in single crystal form but also in crystal aggregation (Fig. 1EF, S10) in comparison to V_pure_0psu. Single crystals exhibited a quadratic dimension with no major crystal pits and aggregated in lenticular, platy globular structures (Fig. 1E, S10). The crystal thickness appeared thicker along the c-axis than for V_pure_0psu (Fig. S9, S10). This observation was also supported by the determined crystallite thickness (LVol-IB) along the c-axis, which was, with 145 nm, larger than for the V_pure_0psu (127 nm, Table S2).

Mg incorporation in the presence of artificial seawater (V_Mg3_9psu, Table 1) changed the crystal morphology in comparison to both Mg-containing vivianite synthesized at freshwater conditions (V_Mg3_0psu) and V_pure_0psu. Single crystals were elongated flattened ellipsoids (Fig. 1H, S11). The edges of the prisma were strongly rounded in comparison to V_pure_0psu (compare Fig. 1A, S9 and 1G, S11) and the edges parallel to the

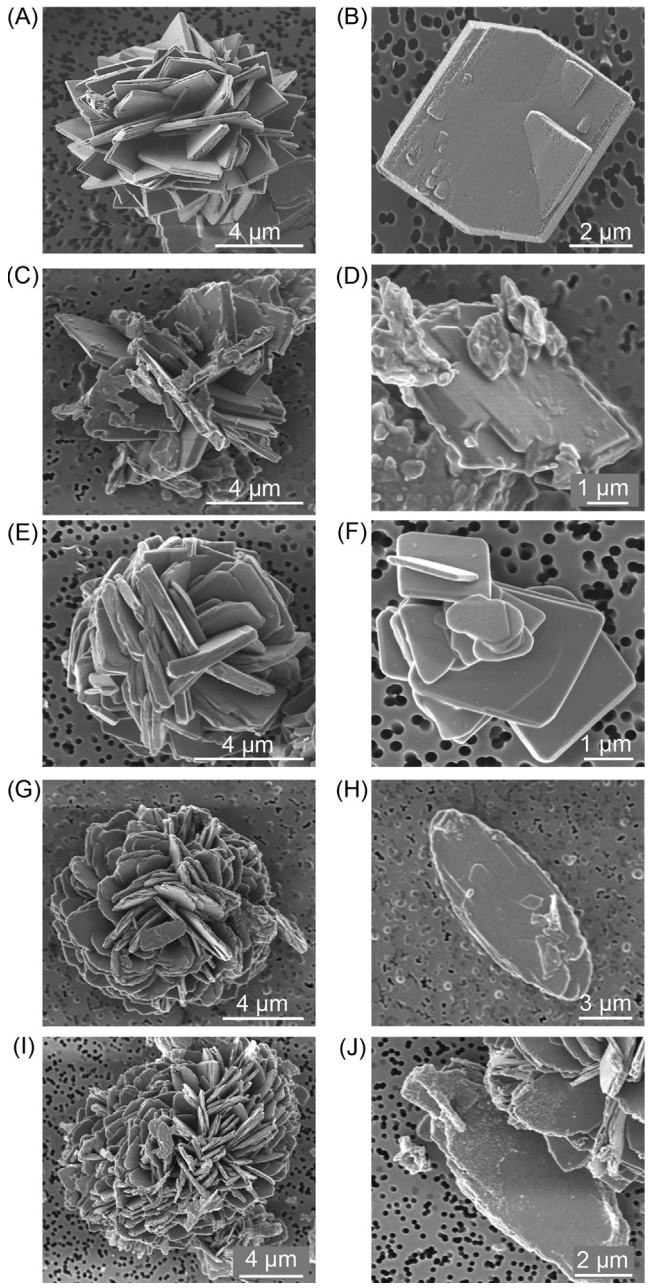


**Fig. 1.** Electron microscopy images of V_pure_0psu (A, B), V_Mn3_0psu (C, D), V_Mg3_0psu (E, F), V_Mg3_9psu (G, H) and V_Mn3_Mg3_9psu (I, J; see Table 1 for synthesis conditions). For each vivianite intergrowth of multiple crystals (left side, rosette structure) and a single crystal (right side) is presented.

(0 1 0) plane were rough. Only very few single crystals were present while the majority of crystals were present in stellate rosettes with bladed structures (Fig. S11). The rosettes were sometimes perfectly globular and had visually a similar crystal size to the V_pure_0psu (Fig. 1AG). However, Rietveld fitting suggested a decrease in crystallite size (LVol-IB) with the incorporation of Mg in presence of seawater (59 nm versus 132 nm, respectively; Table S2). Additionally, crystals appeared visually thinner along the c-axis than V_pure_0psu and V_Mg3_0psu, which was also supported by the single peak fit along the (0 1 0) plane (57 nm versus 127 and 145 nm, respectively; Table S2).

The addition of Mn besides Mg at salinity of 9 psu (V_Mn3_Mg3_9psu, Table 1) led to crystals looking similar to V_Mg3_9psu (Fig. 1G–J, S14) but with some differences noted. Firstly, crystals had a flattened elongated rhomboid shape (Fig. 1J). Secondly, crystal edges were not rounded and rosettes appeared to be less densely packed (Fig. 1I, S14). Nevertheless, rough edges on crystal terraces were visible and the crystals appeared flakier (Fig. 1I, S14). Additionally, rosettes were smaller (~10 µm) than V_pure_0psu (Fig. 1G, S14). The crystallite size determined by Rietveld fitting supported the observation of smaller crystal size in comparison to V_pure_0psu (64 nm versus 132 nm; Table S2).

### 3.2. Bulk composition of substituted vivianites

All synthesized solid-phase precipitates had a molar ratio of (Fe+Mn+Mg)/P of 1.55–1.65 (Table 1) based on acid dissolution followed by ICP-OES analysis. Molar ratios derived by EDX measurements were generally in line with ICP-OES ratios (Table S4). Thermodynamic equilibrium calculations indicated that all synthesis solutions containing artificial seawater were also supersaturated in respect to various amorphous calcium-phosphate mineral phases and hydroxyapatite in addition to vivianite. In the presence of Mn and/or Mg, the solution was also supersaturated in respect to $MnHPO_4$(s) and/or $MgHPO_4{\cdot}3H_2O$(s). XRD data (see Section 3.3) suggested only the formation of a Mn-phosphate mineral phase. Hence, we do not further discuss the potential formation of other mineral phases.

Based on thermodynamic equilibrium calculations, the dominant Mn species were $MnHPO_4$ followed by $Mn^{2+}$, $MnSO_4$ and $MnCl^+$ in the varying syntheses conditions (Table S1). Manganese present as $MnHPO_4$ declined from ~69% (for V_Mn3_0psu) to ~58% (for V_Mn3_Mg3_9psu) with increasing salinity, while the contribution of the other three species increased (Fig. S2EF, Table S1). At all co-precipitation conditions, aqueous Mn was completely incorporated into the solid-phase precipitate (Fig. 2A). Neither the presence of Mg nor changes in salinity influenced Mn incorporation into the solid-phase precipitate. The determined Mn/(Fe+Mn) ratios in Mn-containing vivianite determined by EDX measurements were with 0.15 and 0.34 for V_Mn1_0psu and V_Mn3_0psu, respectively, generally in line with the ratios quantified by ICP-OES (0.14 and 0.31, respectively, Table S4).

The chemical speciation of Mg changed in the presence of artificial seawater differently to the Mn speciation (Table 1, S1, Fig. S2A–D). At the highest Mg concentration at 0 psu, ~38% and 2% of Mg was calculated to be present as $MgHPO_4$ and $MgCl^+$, respectively. At 9 psu, less Mg was complexed to orthophosphate (~30%), while more Mg was complexed to chloride (~7%). The contributions of $Mg^{2+}$ and $MgSO_4$ were not substantially affected by changes in salinity. The presence of Mn led to a further reduction in $MgHPO_4$ complexes to about ~23% and an increase in $MgCl^+$ complexes to about ~9 % (Table 1, S1, Fig. S2A–D). Similar to changes in Mg speciation in the presence of artificial seawater, Mg incorporation into the solid-phase precipitate changed with salinity. At 0 psu, aqueous Mg was completely incorporated into the solid-phase precipitate (Fig. 2B). However, with increasing salinity a decrease in Mg incorporation into the solid phase was evident (Fig. 2B). At 0 psu, an initial aqueous Mg/(Mg+Fe) molar ratio of 0.35 led to a solid phase molar ratio of 0.34. In contrast, at 9 psu, an initial aqueous Mg/(Mg+Fe) molar ratio of 0.35 resulted in a solid phase molar ratio of 0.23. Thus, with increasing salinity Mg incorporation into the solid phase decreased by ~35%. In contrast to salinity, the presence of Mn in the aqueous solution did not affect Mg incorporation into the solid phase at varying salinity (Fig. 2C). Only at the highest Mn concentration (Mn/(Mn+Fe) = 0.35 M ratio) and a salinity of 9 psu was a slight decrease in Mg incorporation detected. Generally, Mg contents in vivianite determined by ICP-OES were larger than Mg contents derived by EDX

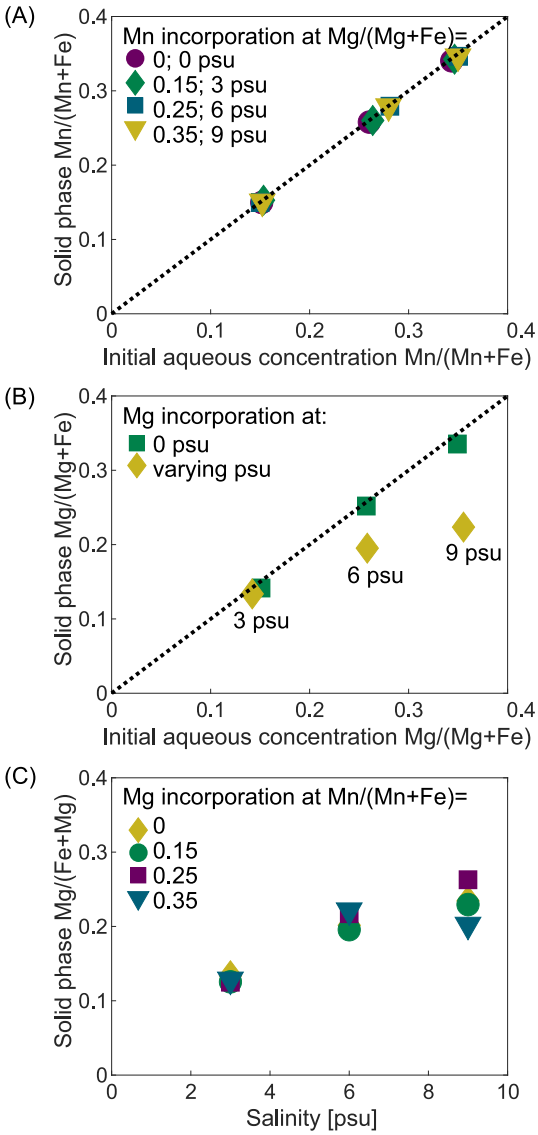


**Fig. 2.** Elemental molar solid phase ratios of substituted vivianites formed at varied initial aqueous concentration ratios and salinity (see Table 1 for syntheses conditions). The dashed lines represent no fractionation of the divalent cations. Panel (A): Incorporation of Mn at four different salinities, translating into varying Mg concentrations. Panel (B): Incorporation of Mg at 0 psu and varying salinity. Panel (C): Incorporation of Mg in the presence of different Mn concentrations at varying salinity. Error bars representing the standard deviation of triplicate dissolutions of the solid phase are not shown as they are smaller than the symbol.

measurements at different vivianite spots (Table S4, for further explanations please refer to Section S4.2).

### 3.3. Changes in crystal structure of substituted vivianites

For all synthesis conditions, the powder XRD patterns of the formed solid-phase precipitate were fitted as vivianite (Table 1, Fig. 3, S4). However, at high initial aqueous Mn concentrations, a second mineral phase was evident in the XRD pattern. The diffraction pattern of the second mineral phase resembled a nanocrystalline, hydrated Mn-phosphate (Fig. 3, S4). The presence of the hydrated Mn-phosphate was detected at synthesis conditions of V_Mn3_0psu, V_Mn3_Mg1_3psu and V_Mn3_Mg2_6psu (Table 1) and contributed 71%, 35% and 24% to the total solid phase, respectively (Table S2). EDX analysis and $^{57}$Fe-Mössbauer spectroscopy (discussed in detail in Section S4, S5) indicated the presence of Fe in the Mn-phosphate phase (Fig. S16, S8, Table S5). The Mn/(Fe+Mn) ratios of the Mn-containing vivianites and the hydrated Mn-phosphate phase derived from the EDX analyses were similar (Fig. S8, Table S5, detailed explanation in Section S4), suggesting an even distribution of Fe and Mn between both mineral phases.

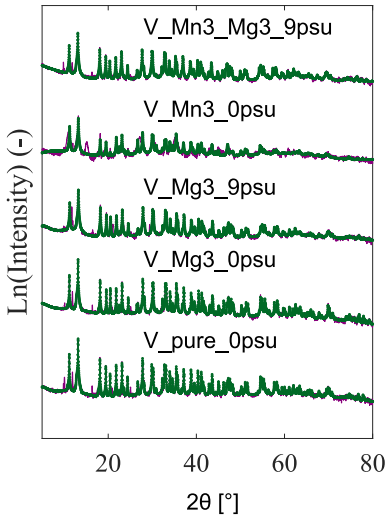


**Fig. 3.** XRD patterns (purple) and Rietveld fits (green) of selected vivianites. XRD patterns and Rietveld fits of all vivianites are presented in Fig. S4. (For interpretation of the references to colour in this figure legend, the reader is referred to the web version of this article.)

The unit cell dimensions of vivianite varied depending on the degree of Mn and/or Mg substitution in the vivianite crystal lattice. The Fe-pure vivianite (V_pure_0psu) had calculated unit cell dimensions of 10.104 Å, 13.450 Å, 4.710 Å and 104.303° for a, b, c and β, respectively. The unit cell dimensions along the a-, b- and c-axis, as well as the angle β increased linearly to maximum values of 10.166 Å, 13.539 Å, 4.730 Å and 104.572°, respectively, with increasing Mn substitution to up to a molar Mn/(Mn+Fe) ratio of 0.34 in the vivianite crystal lattice (Fig. 4, Table S2). In contrast to Mn-containing vivianites, Mg substitution did not change the unit cell dimensions along the a- and b-axis in comparison to V_pure_0psu (Fig. 4). However, the unit cell dimensions along the c-axis decreased linearly from 4.710 Å with no Mg substitution to 4.687 Å with increasing Mg substitution (maximum of 0.34 Mg/(Mg+Fe) ratio; Fig. 4). Additionally, β widened linearly with Mg-substitution from 104.304 Å to 104.642 Å when vivianite had a molar ratio of 0.34 Mg/(Mg+Fe) (Fig. 4), comparable to the trend seen for Mn-substituted vivianites (Fig. 4). When both Mn and Mg were incorporated into the vivianite crystal lattice, no consistent changes along the a-, b- and c-axis of the unit cell were observed (Fig. S5). However, increasing Mn and Mg contents led to a widening of β from 104.303° to 104.653° (Fig. S5).

The quantified Mg-content by Rietveld fitting (Table S3) was somewhat lower than the Mg-content determined by acid dissolution (Table 1, S4). Nevertheless, the general trends in molar ratios were coherent. For instance, acid dissolution estimated Mg/(Fe+Mg) ratios of 0.14, 0.25 and 0.34 for V_Mg1_0psu, V_Mg2_0psu and V_Mg3_0psu, respectively, while Rietveld fitting determined 0.11, 0.15 and 0.25, respectively (Table S3).

### 3.4. Local Fe coordination and position of substituting cations

Incorporation of Mn and Mg into vivianite resulted in changes in the crystal morphology of vivianite. To unravel changes on the atomic scale, Fe K-edge XAS analysis and $^{57}$Fe-Mössbauer spectroscopy were applied in addition to XRD.

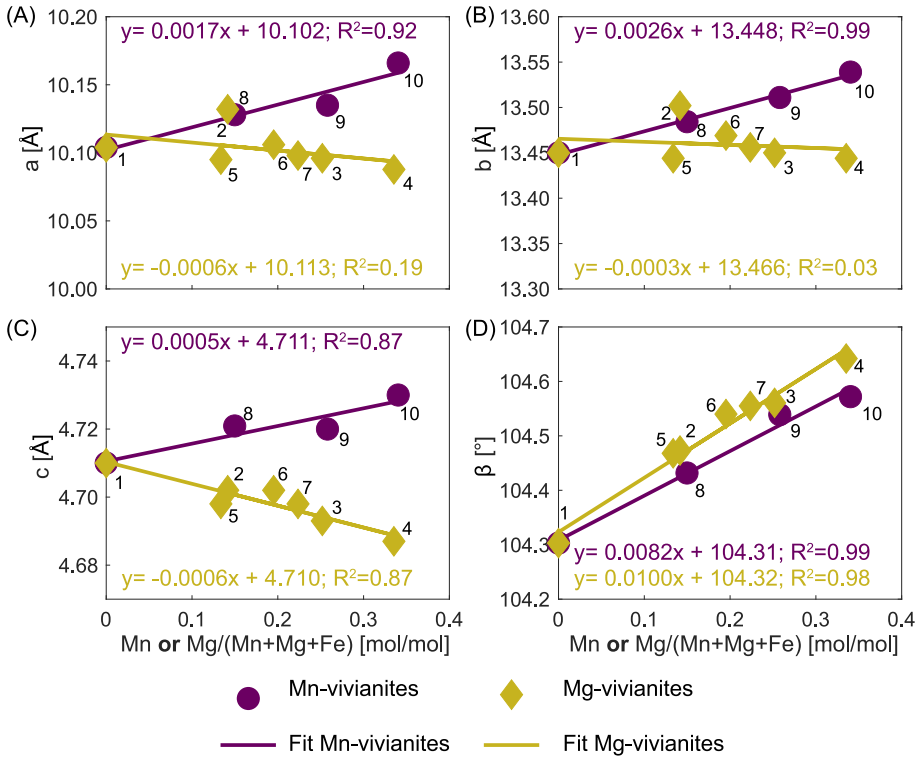


**Fig. 4.** Changes in unit cell dimensions of vivianite with Mn or Mg incorporation into vivianite. The numbers in the figures correspond to the vivianite numbers of the different vivianites presented in Table 1.

The Fourier-transformed $k^3$-weighted Fe K-edge EXAFS spectra of the V_pure_0psu, V_Mg3_0psu, V_Mg3_9psu and V_Mn3_Mg3_9psu resembled each other (Fig. 5, S17). The first-neighbor shell of all four vivianites was fitted with a Fe–O path with a distance of 2.11–2.29 Å (Table 2), followed by a Fe–Fe and Fe–P path in the second-neighbor shell with a distance of ca. 3.00 and 3.30 Å, respectively. The third-neighbor shell was fitted with a Fe–O path and multi-scattering Fe–O–O path with ca. 4.00 and 4.46 Å distance, respectively. The fourth, fifth and sixth-neighbor shells were fitted by Fe–Fe paths with distances of ca. 4.67, 5.25, 5.57 and 6.22 Å (Table 2). The addition of a forward triangle multiple scattering Fe–O–O path with a distance of ca. 4.46 Å and single scattering Fe–Fe paths with distances of ca. 5.25 Å and 5.57 Å improved the fits, which was verified by the application of F-Tests based on determined R-factors to compare different fitting models (Table S7, Downward et al., 2007; Ravel and Newville, 2005). While V_pure_0psu, V_Mg3_0psu and V_Mg3_9psu had similar fitted interatomic path distances, simultaneous incorporation of Mn and Mg into the vivianite structure (V_Mn3_Mg3_9psu) resulted in interatomic path distances deviating more by either being larger, for instance in case of the first Fe–O path (2.29 vs 2.12 Å), or smaller (Fe–P path of 3.09 vs 3.34 Å Table 2).

While interatomic path distances were generally not greatly impacted by Mn and Mg substitution, the path CNs were reduced (Table 2), which was visible by a reduction of shell magnitude (Fig. 5, S17). The CN of V_pure_0psu for the first neighboring shell was fixed to 6 (Fe–O) and CN values of ca. 1.2, 3.9, 1.9, 3.0 and 6.5 were fitted for Fe–Fe1-5 paths, respectively. Incorporation of Mn and/or Mg resulted in a reduction in CN of the first neighboring shell (Fe–O) from 5.9 to 5.7 (Table 2). Depending on the substituting cation, the value of CN of the Fe–Fe paths decreased differently. Increasing Mg content led to a reduction of the CN of the Fe–Fe paths. For instance, the Fe–Fe4 path of V_pure_0psu had a CN of 3.0, while V_Mg3_9psu and V_Mg3_0psu had CN values of 2.1 and 1.6, respectively (Table 2). Simultaneous incorporation of Mn and Mg (V_Mn3_Mg3_9psu) resulted in CN values lower than V_pure_0psu but higher than V_Mg3_9psu. For instance, the Fe–Fe5 path of V_pure_0psu had a CN value of 6.6, while V_Mn3_Mg3_9psu and V_Mn3_Mg3_9psu had CN values of 4.9 and 4.5, respectively (Table 2).

The Fourier-transform of the Fe K-edge EXAFS spectra of V_Mn3_0psu differed from the other four vivianite spectra, in agreement with the presence of another mineral phase as previously discussed. Thus, the Fe-EXAFS shell-fit of V_Mn3_0psu contained different fitted paths and the results were not interpretable regarding the effect of Mn substitution on the vivianite structure. Neighboring shell paths, which were also fitted for V_pure_0psu (Fe–O1, Fe–Fe1, Fe–P, Fe–O-O, Fe–Fe2 and Fe–Fe5, Table 2), had similar interatomic distances than for V_pure_0psu. Additionally, Fe–Mn paths with distances of ca. 3.6 Å and ca. 5.0 Å were included, which were derived with FEFF6 (Zabinsky et al., 1995) from $Mn_3(PO_4)_2{\cdot}3H_2O$ (JCPDS card no. 00-003-0426). The CNs of V_Mn3_0psu were substantially lower than the CNs of V_pure_0psu and the other substituted vivianites. For instance, the CN of the first neighboring shell was only 4.9, while for the other four vivianite samples the CN was above 5.7 (Table 2).

While shell fits of Fe K-edge EXAFS spectra provide insights into interatomic distances and CN of fitted paths, $^{57}$Fe-Mössbauer spectroscopy is a complementary tool since it can differentiate between the Fe bound in the $Fe_A$ and $Fe_B$ position in the vivianite structure. All measured vivianites were fitted with three doublets (Fig. 6a, S15). The corresponding hyperfine parameters are presented in Table S6. Two doublets represented the $Fe_A$ and $Fe_B$ site, which had isomer shift (IS) and quadrupole splitting (QS) values typical for vivianite (Dyar et al., 2014; Etique et al., 2021). A third doublet was included in the fit, which had smaller IS and QS values of ~0.6 mm/s and 0.5–0.8 mm/s, respectively. These values are typical for Fe(III). The contribution of Fe(III) was, for all vivianites,

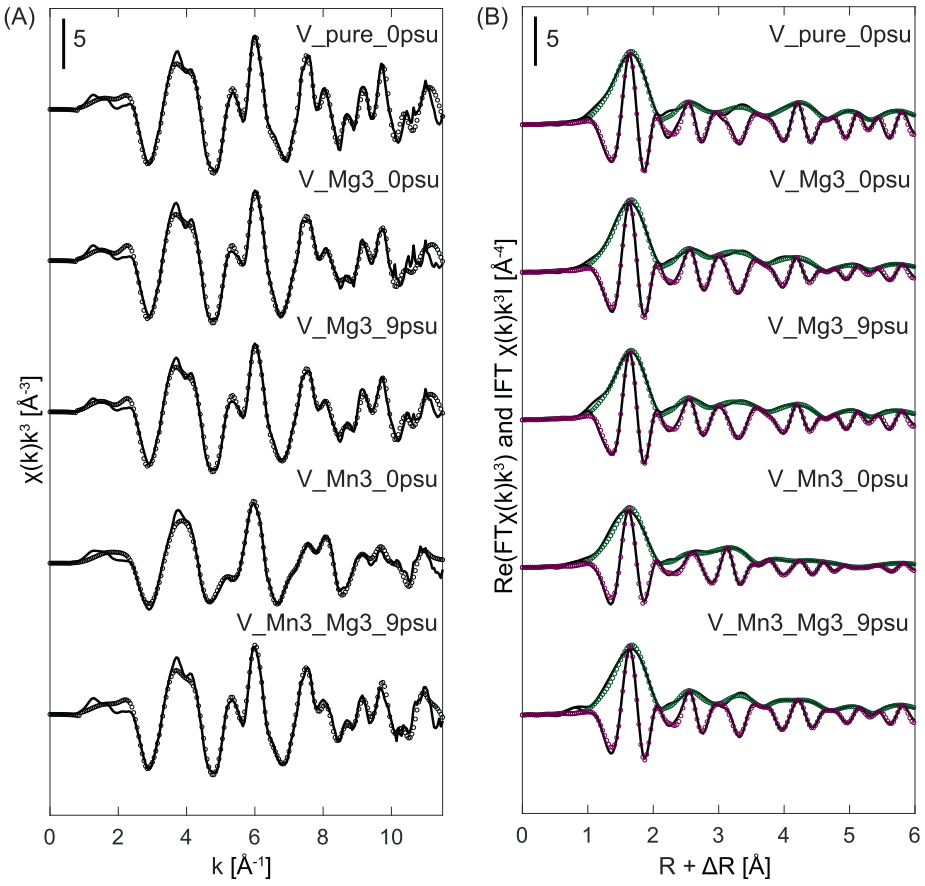


**Fig. 5.** (A) Fe K-edge EXAFS spectra and (B) magnitudes and real parts of Fourier-transform of $k^3$-weighted Fe K-edge EXAFS spectra of pure and Mn- and/or Mg- substituted vivianites. Solid lines indicate experimental data and dotted lines show the shell-fit models (Fe K-edge EXAFS spectra in black; magnitude and real parts of Fourier-transformed $k^3$-weighted Fe K-edge EXAFS spectra in green and purple, respectively). The corresponding EXAFS parameters are reported in Table 2. (For interpretation of the references to colour in this figure legend, the reader is referred to the web version of this article.)

below 10%. The Fe-pure vivianite V_pure_0psu had an IS and QS of 1.32 mm/s and 2.64 mm/s, respectively, for the $Fe_A$ position and an IS and QS of 1.36 mm/s and 3.24 mm/s, respectively, for the $Fe_B$ position (Table S6). No substantial changes in IS and QS were detected with incorporation of Mn and/or Mg in the vivianite crystal lattice, which resulted in $^{57}$Fe-Mössbauer spectra of close resemblance for all vivianites (Fig. 6A–C, S15).

As $^{57}$Fe-Mössbauer spectroscopy can be used to detect changes in the ratio of the $Fe_B$ to $Fe_A$ area, it can provide insights into changes in Fe distribution with changes in Mn and/or Mg content in the vivianite crystal lattice. The theoretical areal ratio between $Fe_B/Fe_A$ position is 2 (McCammon and Burns, 1980). If Mn and Mg are incorporated stoichiometrically into both atom positions, the ratio should be unchanged with substitution in respect to the ratio of V_pure_0psu.

For calculating the ratio of Fe bound in the $Fe_A$ and $Fe_B$ position, we stoichiometrically distributed the present Fe(III) to the two different Fe positions, since at low ferric concentrations (Fe(III) < 10%) oxidation rates between the two different crystallographic sites show little deviation from a 2:1 ratio (McCammon and Burns, 1980). Thus, one third of the Fe(III) area contribution was added to the $Fe_A$ area, while the remaining Fe(III) contribution was added to the $Fe_B$ area. In V_pure_0psu, the $Fe_B$ to $Fe_A$ ratio was 1.70 (Fig. 6A) and hence, rather close to the theoretical ratio of 2. With decreasing Fe content and corresponding increase in Mn and/or Mg content in vivianite, the ratio of $Fe_B$ to $Fe_A$ decreased linearly. For instance, when 44% of the Fe was replaced by Mn and Mg, the ratio was ~1.43 (Fig. 6D), indicating that the contribution of Fe bound in the $Fe_B$ position decreased relative to the $Fe_A$ position with increasing substitution.

## 4. Discussion

### *4.1. Effects of isomorphic substitution on crystal size and morphology of vivianite*

The Fe-pure vivianite (V_pure_0psu) had an elemental composition (Table 1) in the range typically reported for vivianite found in the environment (Egger et al., 2015; Rothe et al., 2016; Lenstra et al., 2018). In addition, V_pure_0psu had unit cell dimensions (Table S2) in agreement with those typically reported for vivianite (Mori and Ito, 1950; Capitelli et al., 2012). As the vivianite crystals had the typical prismatic form, well-defined cleavage along the (010) surface and formed rosette and florets structures (Rothe et al., 2016), we define V_pure_0psu as our reference material to discuss the effects of Mn and/or Mg substitution and salinity.

Generally, crystal(lite) size decreased with substitution (Fig. 1, Table S2) and crystals exhibited more pits and roughness as well as modified crystal aggregation with Mn and/or Mg substitution (Fig. 1, S9–S14). These changes point towards a disruption in crystal growth with changes in crystallinity due to divalent cation substitution. Additionally, the overall increase in metal availability at synthesis conditions with Mn and/or Mg present, could have led to a more rapid precipitation of vivianite also resulting in a decrease in crystallinity. Differences in crystal morphology were

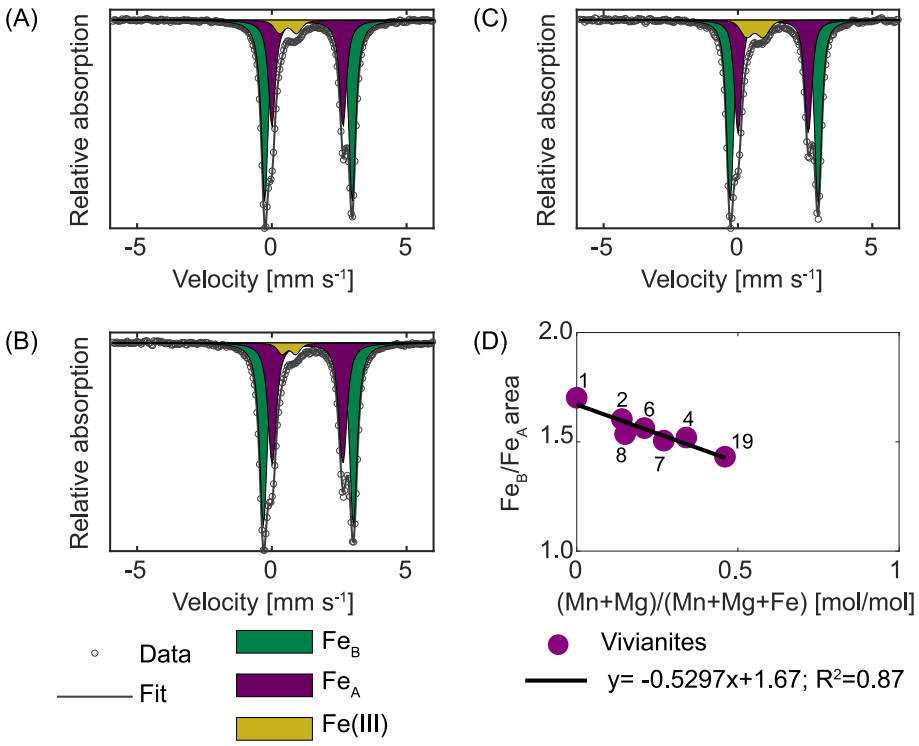


**Fig. 6.** $^{57}$Fe-Mössbauer spectra of V_pure_0psu (A), V_Mn3_Mg3_9psu (B) and V_Mg3_0psu (C) with the fit of the different Fe positions. Additional spectra can be found in the Supplementary data (Fig. S15). Fit parameters are detailed in Table S6. (D) Change in areal $Fe_B$ to $Fe_A$ ratio with changing Fe content. The numbers correspond to the different vivianites (Table 1).

also observed depending on the salinity during the precipitation and growth of the crystals.

No major changes in the crystal habit of Mn-containing vivianite, suggests that Mn incorporation does not affect crystal growth substantially, by for instance inhibiting one particular growth direction relative to another (Fig. 1, S12, S13). In contrast, Mg incorporation at freshwater conditions resulted in a different crystal habit. An increase in crystal thickness in crystallographic c-direction (Fig. 1, S10, Table S2) with Mg incorporation suggests that the presence of Mg inhibits crystal growth in the crystallographic b-direction relative to growth in crystallographic c-direction. The inhibition of one growth direction relative to another growth direction due to Mg has also been shown for calcite (Folk, 1974; Davis et al., 2000). Step-pinning and blocking as well as incorporation may explain the changes in crystal growth patterns. Information about the step advancement rate would be needed to identify the process behind the change in crystal growth, leading to the observed change in crystal morphology (Davis et al., 2000; Yoreo, 2003). Interestingly, when Mg was incorporated in the presence of artificial seawater, the crystal habit differed substantially from the effect observed during Mg substitution at freshwater conditions. The crystals were thinner, elongated, and edges were rounded (V_Mg3_9psu, Fig. 1, S11). While the edges seemed more rounded, the terraces appeared rougher (Fig. S10 vs S11). The observed changes in the presence of artificial seawater are likely caused by the other constituents present in artificial seawater such as Ca and K, which might block kink sites and therefore alter crystal growth (Yoreo, 2003). The blocking of kink sites by, for instance, Ca might have also led to an incorporation of Ca into the crystal structure which could be a potential explanation why Ca was detected in minor amounts by ICP-OES measurements of the acid-digested minerals (see Supplementary data). Generally, the crystals of V_Mg3_9psu (Fig. 1, S11) are similar to vivianite found in the environment (Rothe et al., 2016; Dijkstra et al., 2016). However, the crystal edges were rounder than of vivianite detected in the environment (O'Connell et al., 2015; Egger et al., 2015). This difference might be related to a rather elevated Mg content, which is uncommon for environmental vivianite. The addition of Mn in the presence of Mg and artificial seawater (V_Mn3_Mg3_9psu), resulted in flakier and less rounded crystals and rosettes appearing less densely packed (Fig. 1, S14). The crystals of V_Mn3_Mg3_9psu looked similar to vivianite found in brackish coastal sediments (Egger et al., 2015; Kubeneck et al., 2021).

The similarity of V_Mg3_9psu and V_Mn3_Mg3_9psu to authigenic vivianite might provide some information on the conditions generally present during vivianite formation in the environment. Specifically, both vivianites were synthesized in the presence of artificial seawater and at circumneutral pH with a high degree of supersaturation (Table 1), which was well above the meta-stable zone (Liu et al., 2018b). In addition, the ratio of potential building cations (Fe, Mn and Mg) to phosphate was around 1 or higher. The impact of aqueous cation to anion ratio on vivianite formation has not yet been evaluated, and it is likely that this information may provide further indications on which conditions are favorable for authigenic vivianite formation.

### *4.2. Impact of salinity on elemental composition of vivianite*

Authigenic vivianite found in the environment frequently contains Mn and Mg besides Fe (Rothe et al. (2016) and references therein). Reports of manganoan-vivianite are more common in brackish coastal environments (Egger et al., 2015; Lenstra et al., 2018; Kubeneck et al., 2021), although Mg is a more omnipresent cation in coastal environments (Kubeneck et al., 2021). Mg-containing vivianite has been mainly reported for marine environments low in Mn (Burns, 1997; Hsu et al., 2014). This

environmental observation led to the hypothesis that Mn incorporation into the vivianite crystal lattice might be favored over Mg incorporation (Kubeneck et al., 2021).

The formed vivianite in this study had, with 1.55 and 1.65, molar ratios of (Fe+Mn+Mg)/P very close to the stoichiometric ratio of 1.5 (Rothe et al., 2016). The deviation in the molar ratio might indicate the adsorption of some cations to the crystal surface. Additionally, since P was in high excess in solution, the crystals might have been Fe/Mn/Mg-terminated and thus the bulk composition is not exactly equal to the total composition due to different surface elemental composition.

Contrary to the previous hypothesis of preferential Mn incorporation into the vivianite crystal lattice (Kubeneck et al., 2021), our results show that Mg and Mn are both equally incorporated at freshwater (0 psu) conditions, whereas Mg incorporation is hampered with increasing salinity (Fig. 2). Thermodynamic equilibrium calculations indicate that the speciation of Mg and Mn changed differently with salinity. While for Mn the contribution of aqueous $MnPO_4$ decreased with a simultaneous increase of aqueous $Mn^{2+}$, changes in Mg speciation resulted in a decrease in $MgHPO_4$ complexes with a simultaneous increase in $MgCl^+$ complexes with increasing salinity (Fig. S2, Table S1). Another important non-P containing complex formation of Mg is with sulfate. The contribution of the $MgSO_4$(aq) complex was similar (15–16 mol%) for all synthesis conditions, including those without artificial seawater as sulfate was also added through the Fe stock solution. Thus, complex formation of Mg with sulfate cannot explain our observed trend of decreasing Mg incorporation with increasing salinity. Overall, we hypothesize that the increase in $MgCl^+$ complexes with increasing salinity limits Mg availability for vivianite incorporation, resulting in lower amounts of Mg in the vivianite structure. Hence, if both cations are present in a coastal system, it is more likely that Mn is incorporated than Mg due to chemical speciation of Mg at higher salinity.

The measurement of the elemental composition of vivianites in environmental samples by acid dissolution or EDX requires to hand pick the vivianite crystals. Analysis by XRD in environmental samples with a high vivianite content could be an alternative method to quantify the elemental composition of vivianite (Rothe et al., 2015). While the XRD peak intensities of vivianite are unaltered if Mn is present in the crystal lattice, Mg is a weaker X-ray backscattering atom than Fe (Colliex et al., 2006). Thus, Mg incorporation into vivianite changes the relative XRD peak intensities, allowing to quantify the occupancy fraction of Mg in the two Fe sites ($Fe_A$ and $Fe_B$) sites and providing insights in the distribution of Mg across both Fe sites. While the quantification of the order of magnitude of Mg content was possible by Rietveld fitting (Table S3), the absolute content determined by Rietveld fitting was generally lower than the Mg content determined by acid dissolution and ICP-OES analysis. Simultaneous changes in unit cell dimensions, as well as crystallite size besides the Mg content might make the accurate quantification of the Mg content more challenging. The modelled occupancy factor for Mg for both Fe sites suggest that Mg is preferentially incorporated in the $Fe_B$ site in the vivianite crystal lattice (Table S3), which is in agreement with the Mössbauer results. This could have implications for the redox reactivity of vivianite (see Section 4.3).

### 4.3. Effects of isomorphic substitution on the crystal structure of vivianite

Analysis by XRD and Fe K-edge XAS analysis allows to gain further insights on how substitution affects the crystal structure of vivianite, complementing the observed changes seen in crystal size and morphology by EM. Incorporation of Mn or Mg altered the unit cell dimensions of the vivianite in element specific ways, showing that both Mn and Mg were incorporated into the crystal lattice. The increase of the unit cell parameters with increasing Mn substitution (V_Mn1_0psu, V_Mn2_0psu, V_Mn3_0psu, Table S2, Fig. 4) has also been observed for Mn-substituted siderite (Liu et al., 2019). Since the effective ionic radii of octahedrally-coordinated divalent Mn is larger than the radii of Fe (0.83 versus 0.78 Å for high spin state, respectively Shannon (1976)), an increase in Mn content translates to an increase of the unit cell parameters. Thus, under the experimental conditions covered by our study, Vegard's law, stating that a linear relation exists at a fixed temperature between crystal lattice dimensions and the concentration of a substituting element (Denton and Ashcroft, 1991) is valid. In contrast to Mn, Mg incorporation resulted in a linear decrease along the c-axis of the unit cell (Fig. 4), which is related to the smaller ionic radii of octahedrally-coordinated divalent Mg than Fe and Mn (0.72 versus 0.78 and 0.83 Å, respectively, (Shannon, 1976)). Due to the opposing effect of Mn and Mg on the unit cell dimensions, simultaneous incorporation of Mn and Mg into vivianite crystal lattice did not alter the unit cell parameters a, b and c in a coherent pattern (Fig. S5). However, the linear widening of β might indicate a general distortion of the unit cell with increasing Mn and/or Mg substitution (Fig. S5D).

Shell fits of the Fe K-edge EXAFS spectra of V_pure_0psu and substituted vivianites were in general agreement with previous studies (Bae et al., 2018; Etique et al., 2021). Substitution changed the unit cell dimensions (Fig. 4, S5, Table S2), which subsequently also alters interatomic distances. However, the change in unit cell dimensions is in the range of 0.5–2%, translating to very small changes in interatomic distances which cannot be resolved by shell fits of the Fe K-edge EXAFS spectra. However, the Fe–Fe1 path (Table 2) represents the interatomic bond distance of the two Fe atoms along the c-axis of the unit cell (Fig. S1). Consequently, changes in the Fe–Fe1 interatomic path distance are directly linked to changes in the c-parameter of the unit cell. As discussed above, Mn substitution led to an increase of the c-parameter, while Mg substitution resulted in a decrease. This observation is in agreement with results of the shell fits of the Fe K-edge EXAFS spectra. Mg-containing vivianites (V_Mg3_0psu and V_Mg3_9psu) had a smaller modelled Fe–Fe1 interatomic path distance than V_pure_0psu, while both Mn-containing vivianites had a larger Fe–Fe1 interatomic path distance (Table 2). These observations based on XRD and Fe K-edge XAS analyses clearly show that Mn and Mg were incorporated into the crystal lattice of vivianite.

The shell fit of V_Mn3_Mg3_9psu of the Fe K-edge EXAFS spectrum indicated greater changes in interatomic distances than for the other substituted vivianites (Table 2, S2). This suggests that double substitution by Mn and Mg resulted in stronger distortion of tetrahedral and octahedral structures in vivianite, resulting in changes in the short-range interatomic distances. This stronger distortion might potentially result from the differing ionic radii and electronegativity potentials of Mn and Mg in comparison to Fe, as has also been calculated for double cation substitution in hydroxyapatite (Tamm and Peld, 2006).

In contrast to interatomic distances, the fitted CN for the Fe–Fe paths decreased with Mg incorporation, as Mg is a weaker X-ray backscattering atom than Fe. The reduction in CN for the Fe–Fe paths can be explained by the incorporation of the different cations, however, it could also be an indication for changes in the short-range crystallinity of vivianite due to substitution. In addition, the reduction of CN of the first shell (Fe–O) path likely indicates a distortion of the octahedra with substitution, which is in particular evident when substitution occurred at higher salinity (Table 2).

As vivianite has two different cation positions with differing reactivity (McCammon and Burns, 1980), it is of particular interest

to identify the atom position in which Mn and Mg are incorporated. The possibility of intervalence charge transfer at the $Fe_B$ position allows the stabilization of a ferrous-ferric ion pair at this position. Thus, at high oxidation levels (Fe(III) above 10%), ferrous iron located in the $Fe_A$ position is preferentially oxidized, while the second ferrous iron in the $Fe_B$ position is stabilized by the close proximity of ferric iron (McCammon and Burns, 1980). This mechanism stabilizes vivianite even under oxic conditions and hinders complete oxidation (Rouzies and Millet, 1993).

The fitted IS and QS values of three fitted doublets (Table S6) are similar to previously published values for vivianite at 77 K (Forsyth et al., 1970; Dyar et al., 2014; Etique et al., 2021). The fitted values of the Fe(III) doublet suggest a heterogeneity regarding the distribution of the Fe(III) across both crystallographic sites (De Grave et al., 1980; Nembrini et al., 1983). As the crystallographic position of the Fe(III) could not be unambiguously determined and oxidation rates between both positions are similar up to a oxidation level of 10% (McCammon and Burns, 1980) we distributed the Fe (III) stoichiometrically across both sites for calculating the area ratio of $Fe_B$ to $Fe_A$. The areal ratio of $Fe_B$ to $Fe_A$ of the Fe-pure vivianite of this study is, with 1.70 closer, to the theoretical ratio of 2 than in previous studies (e.g. 1.53 in Etique et al. (2021), ratio calculated similarly to this study). As the ratio is smaller than the theoretical ratio, this suggests the presence of vacancy sites in the $Fe_B$. Furthermore, based on the $^{57}$Fe -Mössbauer data (Fig. 6) Mn and Mg appear to be preferentially incorporated in the $Fe_B$ position. Quantification of Mg by Rietveld fitting of the XRD pattern also indicated a higher Mg content in the $Fe_B$ position (Table S3). Our data are thus coherent with observations by Yakubovich et al. (2001) who also concluded that Mg prefers to be present in the double octahedron in Fe-substituted baricite, the Mg-end member of the vivianite mineral group. As discussed before, the presence of Mg and Mn could impact the intervalence charge transfer in the double octahedral site, in particular the higher the Mg and/or Mn content is.

Since Mn is, as Fe, a transition metal, it could carry out intervalence charge transfer. Thus, substitution of Mn should result in heteronuclear intervalence charge transfer between Mn and Fe. Consequently, Mn substitution might not alter the stability and thus redox behavior of vivianite. On the other hand, substitution by Mg might result in a hampering of intervalence charge transfer since Mg only exists in one oxidation state. Hence, heteronuclear charge transfer between Mg and Fe is not possible and substantial substitution of Mg might result in changes in redox reaction rates and destabilization of the vivianite structure under oxidizing conditions. To validate this hypothesis the redox reactivity of Mn and Mg-enriched vivianite should be subject of future research.

### *4.4. Environmental implications of divalent cation substitution in vivianite*

Our results show that the elemental composition of vivianite depends on the composition of the aqueous solution from which it was formed. Our data suggest that changes in Mg speciation with salinity result in the preferential incorporation of Mn over Mg into vivianite at high salinity. This may explain why Mn incorporation is more common in vivianite found in coastal environments. In case of excess P to Fe in aqueous solution, as in this study, the presence of Mn and Mg can facilitate vivianite formation by substituting for Fe in the crystal lattice and thus enhance P removal from aqueous solution.

Furthermore, we show that salinity and incorporation of Mn and/or Mg during crystal growth strongly influences the morphology of crystals and their crystal size. Environmental samples are often treated for instance to size-specific sieving prior to detection and identification of vivianite by EM or XRD (Egger et al., 2015; Rothe et al., 2016; Kubeneck et al., 2021). Ignoring certain fractions of a sample might result in missing vivianite crystals since crystal sizes and aggregation forms change with substitution of Fe. In particular, Mg substitution can change crystal morphology, making identification and quantification of vivianite in environmental samples even more challenging.

Incorporation of other divalent cations affects the interfacial tension in crystals and thus the solubility of minerals (Prieto, 2009). Results for Mn-containing vivianite by Tessenow (1974) indicate changes in solubility with Mn incorporation. Additionally, changes in dissolution rates due to isomorphic substitution in Fe minerals has been frequently reported (Torrent et al., 1987; Alvarez et al., 2008; Ekstrom et al., 2010). Considering that a wide range of elemental contents of Mn and Mg, but also other divalent cations such as Zn, have been reported in natural vivianite (Rothe et al., 2016), a further investigation of changes in solubility due to isomorphic substitution is important to assess the stability of vivianite as a permanent P burial sink. Furthermore, Mn/Mg-containing vivianite formed in artificial seawater exhibited crystal surface roughness, crystal pits, thinner crystals, and likely due to its different aggregation, a different surface area than Fe-pure vivianite, potentially further changing the reactivity of vivianite. Changes in reactivity could include surface reactions such as sorption of metal(loid)s (Thinnappan et al., 2008; Bae et al., 2018) and reduction of metal(loid)s and chlorinated organic compounds (Veeramani et al., 2011; Etique et al., 2021). In addition, the stability of vivianite towards sulfide is a frequently discussed topic in literature due to the potential future production of sulfide in currently non-sulfidic environments as a consequence of sea level rise (O'Connell et al., 2015; Dijkstra et al., 2018; Lenstra et al., 2018; Kubeneck et al., 2021). As vivianite rapidly dissolves in the presence of sulfide based on laboratory experiments (Dijkstra et al., 2018; Wilfert et al., 2020), the expectation of vivianite as a permanent P burial sink could be altered. As Mn and Mg have a lower reactivity towards sulfide than Fe (Thamdrup et al., 1993), substitution of Fe by other divalent cations might change the reactivity of vivianite towards sulfide. Furthermore, our results show a preferred substitution of Mn and Mg in the $Fe_B$ position. Whereas Mn can conduct with Fe heteronuclear intervalence charge transfer, Mg cannot share electrons. Thus, the incorporation of Mn and/or Mg could change the susceptibility of vivianite towards oxidation. This could result in a destabilization of vivianite in environments experiencing changes in redox conditions over time, such as periodically flooded soils and wetlands. It could also be of importance for technical applications such as using the oxidation of vivianite as a slow-release Fe and P fertilizer (Yang et al., 2022).

Overall, our results show that salinity had a strong impact on the isomorphic substitution of Mn and Mg in the vivianite structure, as well as on crystal structure, size and morphology; changes which may have further consequences for the stability and reactivity of vivianite in the environment. In addition, only by using a complex multi-component system such as artificial seawater were we able to form vivianite crystals resembling vivianite found in the environment. Thus, to ensure a better application of laboratory results to the field, future studies investigating the reactivity of vivianite in the environment should include environmentally relevant isomorphic substituted vivianites in addition to Fe-pure vivianite.

## 5. Conclusions

We present a detailed investigation on how crystal characteristics of vivianite change with structural incorporation of Mn and/or Mg in the crystal lattice. We identify the impact of salinity on the Mn and/or Mg incorporation in vivianite. With increasing salinity

(studied up to 9 psu), aqueous Mg speciation changes while Mn speciation is much less affected, potentially explaining the preferred uptake of Mn over Mg in the vivianite crystal structure at high salinity. Both Mn and Mg are preferentially incorporated in the $Fe_B$ position in the vivianite crystal structure independent of salinity, potentially affecting the redox-stability of vivianite. In combination with observed changes in crystallinity, crystal size and morphology, environmental reactivity and stability of vivianite might be altered with divalent cation substitution, requiring further investigation to better assess the stability of vivianite as a permanent P burial sink.

## Declaration of Competing Interest

The authors declare that they have no known competing financial interests or personal relationships that could have appeared to influence the work reported in this paper.

## Acknowledgment

We are grateful to Kurt Barmettler (ETH Zürich) for assisting with laboratory analyses. We thank Giulia Fantappiè (ETH Zürich) for helpful discussions. We thank Ki Tae Nam (Seoul National University) for providing as the CIF file for $Mn_3(PO_4)_2{\cdot}3H_2O$ mineral phase (JCPDS card no. 00-003-0426). We acknowledge SOLEIL (Proposal no. 20190784) for the provision of synchrotron radiation facilities and thank D. Vantelon (SOLEIL, Lucia beamline) for their support during the synchrotron measurements. We further acknowledge the Scientific Center for Optical and Electron Microscopy (ScopeM) of the ETH Zürich for providing access to their microscopes. We would further like to thank the three anonymous reviewers for the insightful and constructive feedback, improving the overall quality of the manuscript. This work received funding from the European Research Council (ERC) under the European Union's Horizon 2020 research and innovation program (grant agreement no. 788009-IRMIDYN-ERC-2017-ADG).

## Appendix A. Supplementary material

The supplementary material contains further information and data on the crystal structure of vivianite, thermodynamic equilibrium calculations, X-ray diffraction, electron microscopy, $^{57}$Fe-Mössbauer spectroscopy and Fe-XAS analysis. Supplementary material to this article can be found online at https://doi.org/10.1016/j.gca.2023.01.029.

## References

Ainsworth, C.C., Girvin, D.C., Zachara, J.M., Smith, S.C., 1989. Chromate adsorption on goethite: effects of aluminum substitution. SSSAJ 53, 411–418.
Allen, G.C., Hush, N.S., 1967. Intervalence-transfer absorption. Part 1. Qualitative evidence for intervalence-transfer absorption in inorganic systems in solution and in the solid state. Prog. Inorg. Chem. 8, 357–389.
Alvarez, M., Rueda, E.H., Sileo, E.E., 2006. Structural characterization and chemical reactivity of synthetic Mn-goethites and hematites. Chem. Geol. 231, 288–299.
Alvarez, M., Sileo, E.E., Rueda, E.H., 2008. Structure and reactivity of synthetic Co-substituted goethites. Am Min 93, 584–590.
Bae, S., Sihn, Y., Kyung, D., Yoon, S., Eom, T., Kaplan, U., Kim, H., Schäfer, T., Han, S., Lee, W., 2018. Molecular identification of Cr(VI) removal mechanism on vivianite surface. Environ. Sci. Tech. 52, 10647–10656.
Berner, R., 1975. The role of magnesium in the crystal growth of calcite and aragonite from sea water. Geochim. Cosmochim. Acta 39, 489–504.
Burns, S.J., 1997. Early diagenesis in Amazon fan sediments. Proc. Ocean Drill. Prog. Sci. Results 155, 531–538.
Capitelli, F., Chita, G., Ghiara, M.R., Rossi, M., 2012. Crystal-chemical investigation of $Fe_3(PO_4)_2{\cdot}8H_2O$ vivianite minerals. Z. Kristallogr. 227, 92–101.
Colliex, C., Cowley, J., Dudarev, S., Fink, M., Gjønnes, J., Hilderbrandt, R., Howie, A., Lynch, D., Peng, L., Ren, G., et al., 2006. Electron diffraction, International Tables for Crystallography. Wiley Online Library, 259–429.
Davis, K.J., Dove, P.M., Yoreo, J.J.D., 2000. The role of $Mg^{2+}$ as an impurity in calcite growth. Science 290, 1134–1137.
De Grave, E., Vochten, R., Desseyn, H., Chambaere, D., 1980. Analysis of some oxidized vivianites. J. phys. Colloq. 41, C1–407.
Denton, A.R., Ashcroft, N.W., 1991. Vegard's law. Phys. Rev. A 43, 3161–3164.
Dijkstra, N., Slomp, C.P., Behrends, T., 2016. Vivianite is a key sink for phosphorus in sediments of the Landsort Deep, an intermittently anoxic deep basin in the Baltic Sea. Chem. Geol. 438, 58–72.
Dijkstra, N., Hagens, M., Egger, M., Slomp, C.P., 2018. Post-depositional formation of vivianite-type minerals alters sediment phosphorus records. BG 15, 861–883.
Dollase, W., 1986. Correction of intensities for preferred orientation in powder diffractometry: application of the March model. J. Appl. Cryst. 19, 267–272.
Downward, L., Booth, C., Lukens, W., Bridges, F., 2007. A variation of the F-Test for determining statistical relevance of particular parameters in EXAFS fits. In: AIP Conference Proceedings. American Institute of Physics, pp. 129–131.
Dyar, M.D., Jawin, E.R., Breves, E., Marchand, G., Nelms, M., Lane, M.D., Mertzman, S. A., Bish, D.L., Bishop, J.L., 2014. Mössbauer parameters of iron in phosphate minerals: Implications for interpretation of martian data. Am. Min. 99, 914–942.
Egger, M., Jilbert, T., Behrends, T., Rivard, C., Slomp, C.P., 2015. Vivianite is a major sink for phosphorus in methanogenic coastal surface sediments. Geochim. Cosmochim. Acta 169, 217–235.
Ekstrom, E.B., Learman, D.R., Madden, A.S., Hansel, C.M., 2010. Contrasting effects of Al substitution on microbial reduction of Fe(III)(hydr)oxides. Geochim. Cosmochim. Acta 74, 7086–7099.
Etique, M., Bouchet, S., Byrne, J.M., ThomasArrigo, L.K., Kaegi, R., Kretzschmar, R., 2021. Mercury reduction by nanoparticulate vivianite. Environ. Sci. Tech., 3399–3407
Folk, R.L., 1974. The natural history of crystalline calcium carbonate: Effect of magnesium content and salinity. J. Sediment. Petrol. 44, 40–53.
Forsyth, J., Johnson, C., Wilkinson, C., 1970. The magnetic structure of vivianite, $Fe_3(PO_4)_2{\cdot}8H_2O$. J. Solid State Phys. 3, 1127.
Froelich, P.N., 1988. Kinetic control of dissolved phosphate in natural rivers and estuaries: a primer on the phosphate buffer mechanism 1. Limnol. Oceanogr. 33, 649–668.
Frost, R., Weier, M., Lyon, W., 2004. Metavivianite an intermediate mineral phase between vivianite, and ferro/ferristrunzite-a Raman spectroscopic study. Neues Jahrb. für Mineral. Abhandlungen 5, 228–240.
Gerth, J., 1990. Unit-cell dimensions of pure and trace metal-associated goethites. Geochim. Cosmochim. Acta 54, 363–371.
Hsu, T.W., Jiang, W.T., Wang, Y., 2014. Authigenesis of vivianite as influenced by methane-induced sulfidization in cold-seep sediments off southwestern Taiwan. J. Asian Earth Sci. 89, 88–97.
Jeon, K., Lee, N., Bae, S., Goddard, W.A., Kim, H., Lee, W., 2015. Theoretical and experimental studies of the dechlorination mechanism of carbon tetrachloride on a vivianite ferrous phosphate surface. Chem. A Eur. J. 119, 5714–5722.
Kester, D.R., Duedall, I.W., Connors, D.N., Pytkowicz, R.M., 1967. Preparation of artificial seawater. Limnol. Oceanogr. 12, 176–179.
Kubeneck, L.J., Lenstra, W.K., Malkin, S.Y., Conley, D.J., Slomp, C.P., 2021. Phosphorus burial in vivianite-type minerals in methane-rich coastal sediments. Mar. Chem. 231, 103948.
Lenstra, W.K., Egger, M., van Helmond, N.A.G.M., Kritzberg, E., Conley, D.J., Slomp, C. P., 2018. Large variations in iron input to an oligotrophic Baltic Sea estuary: Impact on sedimentary phosphorus burial. BG 15, 6979–6996.
Liu, J., Cheng, X., Qi, X., Li, N., Tian, J., Qiu, B., Xu, K., Qu, D., 2018b. Recovery of phosphate from aqueous solutions via vivianite crystallization: Thermodynamics and influence of pH. Chem. Eng. Technol. 349, 37–46.
Liu, H., Lu, X., Li, M., Zhang, L., Pan, C., Zhang, R., Li, J., Xiang, W., 2018a. Structural incorporation of manganese into goethite and its enhancement of Pb(II) adsorption. Environ. Sci. Tech. 52, 4719–4727.
Liu, H., Shu, D., Sun, F., Li, Q., Chen, T., Xing, B., Chen, D., Qing, C., 2019. Effect of manganese substitution on the crystal structure and decomposition kinetics of siderite. J. Therm. Anal. Calorim. 136, 1315–1322.
McCammon, C.A., Burns, R.G., 1980. The oxidation mechanism of vivianite as studied by Mössbauer spectroscopy. Am. Min. 65, 361–366.
Mori, H., Ito, T., 1950. The structure of vivianite and symplesite. Acta Crystallogr. 3, 1–6.
Nembrini, G., Capobianco, J., Viel, M., Williams, A., 1983. A Mössbauer and chemical study of the formation of vivianite in sediments of Lago Maggiore (Italy). Geochim. Cosmochim. Acta 47, 1459–1464.
O'Connell, D.W., Jensen, M.M., Jakobsen, R., Thamdrup, B., Andersen, T.J., Kovacs, A., Hansen, H.C.B., 2015. Vivianite formation and its role in phosphorus retention in Lake Ørn, Denmark. Chem. Geol. 409, 42–53.
Prieto, M., 2009. Thermodynamics of solid solution aqueous solution systems. Rev. Mineral. Geochem., 47–85
Rancourt, D., Ping, J., 1991. Voigt-based methods for arbitrary-shape static hyperfine parameter distributions in Mössbauer spectroscopy. Nucl. Instrum. Methods Phys. Res. B 58, 85–97.
Ravel, B., Newville, M., 2005. ATHENA, ARTEMIS, HEPHAESTUS: Data analysis for X-ray absorption spectroscopy using IFEFFIT. J. Synchrotron Rad. 12, 537–541.
Rothe, M., Kleeberg, A., Grüneberg, B., Friese, K., Pérez-Mayo, M., Hupfer, M., 2015. Sedimentary sulphur:iron ratio indicates vivianite occurrence: A study from two contrasting freshwater systems. PLoS One 10, 1–18.

Rothe, M., Kleeberg, A., Hupfer, M., 2016. The occurrence, identification and environmental relevance of vivianite in waterlogged soils and aquatic sediments. Earth Sci. Rev. 158, 51–64.
Rouzies, D., Millet, J.M., 1993. Mössbauer study of synthetic oxidized vivianite at room temperature. Hyperfine Interact. 77, 19–28.
Ruttenberg, K., 2003. The global phosphorus cycle. Treatise Geochem. 8, 682.
Shannon, R.D., 1976. Revised effective ionic radii and systematic studies of interatomic distances in halides and chalcogenides. Acta Crystallogr. A 32, 751–767.
Stumm, W., Morgan, J.J., 2012. Aquatic chemistry: Chemical equilibria and rates in natural waters, volume 126. John Wiley & Sons.
Tamm, T., Peld, M., 2006. Computational study of cation substitutions in apatites. J. Solid State Chem. 179, 1581–1587.
Tang, J., Niedermayr, A., Köhler, S.J., Böhm, F., Kısakürek, B., Eisenhauer, A., Dietzel, M., 2012. $Sr^{2+}/Ca^{+1}$ and $^{44}Ca/^{40}Ca$ fractionation during inorganic calcite formation: III. Impact of salinity/ionic strength. Geochim. Cosmochim. Acta 77, 432–443.
Tessenow, U., 1974. Reaction mechanisms and equilibria in the system iron manganese-phosphate with regard to the accumulation of vivianite in Lake Ursee. Arch. Hydrobiol. Suppl. 47, 1–79.
Thamdrup, B., Finster, K., Hansen, J.W., Bak, F., 1993. Bacterial disproportionation of elemental sulfur coupled to chemical reduction of iron or manganese. AEM 59, 101–108.
Thinnappan, V., Merrifield, C.M., Islam, F.S., Polya, D.A., Wincott, P., Wogelius, R.A., 2008. A combined experimental study of vivianite and As(V) reactivity in the pH range 2–11. Appl. Geochem. 23, 3187–3204.
Torrent, J., Schwertmann, U., Barron, V., 1987. The reductive dissolution of synthetic goethite and hematite in dithionite. Clay Miner. 22, 329–337.
Trolard, F., Tardy, Y., 1987. The stabilities of gibbsite, boehmite, aluminous goethites and aluminous hematites in bauxites, ferricretes and laterites as a function of water activity, temperature and particle size. Geochim. Cosmochim. Acta 51, 945–957.
Veeramani, H., Alessi, D.S., Suvorova, E.I., Lezama-Pacheco, J.S., Stubbs, J.E., Sharp, J. O., Dippon, U., Kappler, A., Bargar, J.R., Bernier-Latmani, R., 2011. Products of abiotic U(VI) reduction by biogenic magnetite and vivianite. Geochim. Cosmochim. Acta 75, 2512–2528.
Wilfert, P., Meerdink, J., Degaga, B., Temmink, H., Korving, L., Witkamp, G.J., Goubitz, K., van Loosdrecht, M.C., 2020. Sulfide induced phosphate release from iron phosphates and its potential for phosphate recovery. Water Res. 171, 115389.
Yakubovich, O.V., Massa, W., Liferovich, R.P., McCammon, C.A., 2001. The crystal structure of baricite, $(Mg_{1.70}Fe_{1.30})(PO_4)_2{\cdot}8H_2O$, the magnesium-dominant member of the vivianite group. Canad. Mineral. 39, 1317–1324.
Yang, S., Yang, X., Zhang, C., Deng, S., Zhang, X., Zhang, Y., Cheng, X., 2022. Significantly enhanced P release from vivianite as a fertilizer in rhizospheric soil: Effects of citrate. Environ. Res., 113567
Yoreo, J.J.D., 2003. Principles of crystal nucleation and growth. Rev. Mineral. Geochem. 54, 57–93.
Zabinsky, S., Rehr, J., Ankudinov, A., Albers, R., Eller, M., 1995. Multiple-scattering calculations of X-ray-absorption spectra. Phys. Rev. B 52, 2995.
Zachara, J.M., Fredrickson, J.K., Smith, S.C., Gassman, P.L., 2001. Solubilization of Fe (III) oxide-bound trace metals by a dissimilatory Fe(III) reducing bacterium. Geochim. Cosmochim. Acta 65, 75–93.